J. Fluid Mech. (1983), *vol.* 132, *pp.* 25–48
Printed in Great Britain

Magnetic-flux transport by a convecting layer – topological, geometrical and compressible phenomena

By WAYNE ARTER[†]

Department of Applied Mathematics and Theoretical Physics, University of Cambridge,
Silver Street, Cambridge CB3 9EW

(Received 29 September 1982)

Numerical calculations by Drobyshevski & Yuferev (1974) of the redistribution of magnetic flux by a Bénard layer with cells of square planform have been extended to higher values of electrical conductivity and to other velocity patterns, using a computer code developed for another purpose. Reconnection does not proceed as they supposed, but leads to overall field enhancement, and although the energy is greater at the bottom, there is as much unsigned flux in the upper half as in the lower half of the layer. However, compressible velocity patterns can concentrate flux at their bases.

1. Introduction

Observation of the Sun reveals a magnetic field heavily distorted by the convective motions in the outer part of its volume. Estimates of magnetic Reynolds number R_{m}, a measure of the importance of convection relative to diffusion, range from 10^6–10^{11}. Such values are beyond the scope of terrestrial laboratory experiments, so the understanding of high-R_{m} physics has mainly been increased by the use of both analytic and computational techniques (see the recent review by Proctor & Weiss 1982).

The solar field is believed to be predominantly toroidal (or horizontal if curvature is neglected) in the deep convection zone as a result of α-ω dynamo action (e.g. Cowling 1982; Gilman 1982; but see also Gilman & Miller 1981). In the small scales of convective motion nearer the top of the zone, the supergranules and granules, isolated regions of hot rising fluid are observed to be surrounded by connected areas of colder falling fluid, so that the two are topologically distinct. It was suggested in a paper by Drobyshevski & Yuferev (1974, hereinafter referred to as DYM), with an appendix by Moffatt, that in this situation 'topological flux pumping' would act to confine the field to the deeper layers.

This paper, using a computer code developed to solve the equations of magnetoconvection (cf. Weiss 1981), extends the Russians' numerical work to higher R_{m} and considers another topologically similar velocity pattern denoted by SSW (after its authors' initials). A parallel investigation in a slightly different geometry has been performed by Galloway & Proctor (1983). Since DYM was published, evidence has mounted that the deeper convective motions are roll-like, elongated in the direction of the rotation axis (Busse 1977, 1978; Gilman 1975, 1980), and rolls cannot produce

---

[†] Present address: Theoretical Physics Division, UKAEA/Culham Laboratory, Abingdon, Oxfordshire OX14 3DB, England.

asymmetries in the distribution of horizontally averaged flux (Arter 1983). As is well known, mixing-length theory predicts there are several pressure scale heights across the zone, so it is important to see what occurs when we relax the incompressibility condition div $\boldsymbol{u} = 0$. We therefore also consider compressible roll-like motion predominantly across magnetic field-lines as a model for these rotationally dominated flows, and take a corresponding motion around fieldlines as a model for situations where the magnetic field is relatively stronger. Such flows will be denoted by $C_\perp$ and $C_\parallel$ respectively.

All four velocity patterns are described in §2, together with what may be analytically inferred about their effect on the distribution of magnetic field $\boldsymbol{B}$. SSW is shown to produce a net *upward* transport of field at low R_m; $C_\perp$ and $C_\parallel$ may be studied in a low-R_m formalism which shows that $C_\perp$ sends flux upwards, $C_\parallel$ flux downwards and there is no transport when motion is symmetric in the horizontal directions. This redistribution of flux by SSW represents the geometrical pumping effect (Proctor 1975), i.e. it depends on the detailed structure of the velocity field, not the topology.

Section 3 describes the computational techniques used to solve the problem at higher R_m, and §4 the result obtained numerically. At larger R_m, the SSW results are increasingly found to resemble those from the Drobyshevski & Yuferev (DY) pattern. This confirms that geometrical pumping is unimportant at high R_m (Proctor 1975; Moffatt 1978, §3.12), when topological effects come into play. The result is not as anticipated by DYM, however, and roughly equal amounts of unsigned flux are seen in the top and bottom halves of the layer (§4.2) and the field is enhanced throughout much of the volume. The dominant magnetic energy feature is nevertheless a bottom flux tube (§4.3). Section 4.4 shows that the low-R_m behaviour of $C_\perp$ and $C_\parallel$ is also reproduced at higher R_m. Section 5 discusses the numerical results in the context of dynamo theory, and further implications are discussed in §6.

2. Analytic results

2.1. *Introduction*

The formal statement of the problem is to solve (for $\boldsymbol{B}$) the magnetic induction equation, which in dimensionless form is

$$\frac{\partial \boldsymbol{B}}{\partial t} = R_\mathrm{m}\,\mathrm{curl}\,(\boldsymbol{u} \wedge \boldsymbol{B}) + \nabla^2 \boldsymbol{B}, \tag{2.1}$$

for a given velocity pattern $\boldsymbol{u}(\boldsymbol{x})$, with $\boldsymbol{B} = (1,0,0)$ at $t = 0$, subject to the (periodic) boundary conditions ((x,y,z) are Cartesian coordinates)

$$B_y = B_z = 0 \quad (x = 0, \lambda),$$

$$\frac{\partial B_x}{\partial y} = \frac{\partial B_z}{\partial y} = B_y = 0 \quad (y = 0, \Lambda),$$

$$\frac{\partial B_x}{\partial z} = \frac{\partial B_y}{\partial z} = B_z = 0 \quad (z = 0, 1).$$

It follows that, if we define $\Phi(x,y,z) = \int_0^y \int_0^z B_x \,\mathrm{d}y\,\mathrm{d}z$,

and let $\Phi_0(x) = \Phi(x, \Lambda, 1)$ then, provided that the normal component of $\boldsymbol{u}$ vanishes on the boundaries of the box $0 \leqslant x \leqslant \lambda$, $0 \leqslant y \leqslant \Lambda$, $0 \leqslant z \leqslant 1$,

$$\left(\frac{\partial}{\partial t} - \frac{\partial^2}{\partial x^2}\right)\Phi_0 = 0.$$

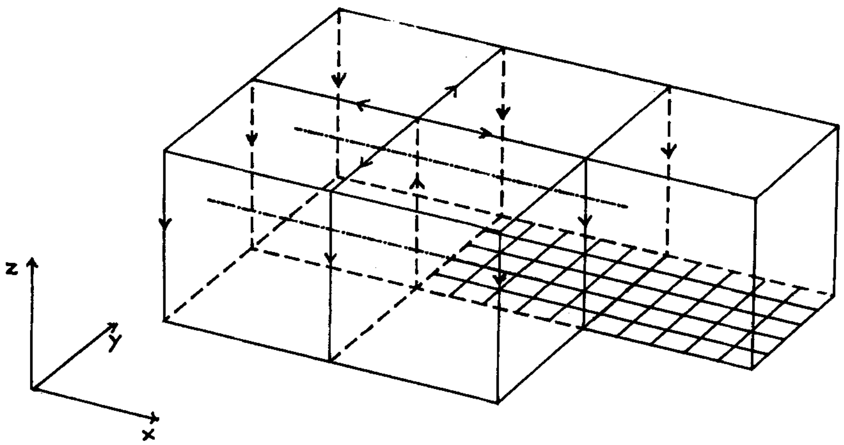

FIGURE 1. Perspective view showing the two incompressible velocity patterns schematically. Initial magnetic-field direction is indicated by the dot-dash lines. The left-hand half of the volume spanned by the hatched base constitutes the 'quarter-cell of symmetry'.

Since $\operatorname{div} \boldsymbol{B} = 0$, Φ_0 is independent of x, implying that Φ_0 is conserved at all times, however much field may rearrange itself on a surface $x =$ constant.

2.2. *Incompressible velocity fields*

The two incompressible velocity fields studied in detail are poloidal, $\boldsymbol{u} = \operatorname{curl}\operatorname{curl}(S\hat{\boldsymbol{z}})$, and satisfy stress-free boundary conditions. They are shown schematically in figure 1. We use a square planform because this provides the simplest representation of the observed small-scale solar convection.

As in DYM, we put $\lambda = \Lambda = 1$, and set

$$S = (\cos \pi x + \cos \pi y + \tfrac{1}{2}\cos \pi x \cos \pi y) \sin \pi z;$$

alternatively, for the pattern given by H. U. Schmidt, G. W. Simon & N. O. Weiss (private communication),

$$S = (\cos \pi x + \cos \pi y - \tfrac{1}{12}[\cos 2\pi x + \cos 2\pi y]) \sin \pi z.$$

These will be referred to as DY and SSW respectively.

Obviously $\boldsymbol{u}$ possesses a symmetry about $z = \frac{1}{2}$. $u_z(x, y, \frac{1}{2})$ for DY has relatively sharp maxima and rounded minima, vice versa for SSW (figure 2). Flowlines, solutions of

$$\frac{\mathrm{d}\boldsymbol{x}}{\mathrm{d}s} = \boldsymbol{u}(\boldsymbol{x}(s)),$$

are plotted in figures 3 (a, b), which suggest they are closed. If we write $S = h(x, y) \sin \pi z$ and seek functions F constant on streamlines of the form $F = f(x, y) \sin \pi z$, then f satisfies

$$\frac{\partial h}{\partial x}\frac{\partial f}{\partial x} + \frac{\partial h}{\partial y}\frac{\partial f}{\partial y} - (\nabla^2 h) f = 0.$$

This equation is invariant under the transformation $x + y \rightarrow x$, $x - y \rightarrow y$. It has solutions $f = l'(x)\, m'(y)$ if $h(x, y) = l(x) + m(y)$ or $h(x, y) = l(x)\, m(y)$; thus flowlines must lie on surfaces $F = f(x, y) \sin \pi z =$ constant, where for DY

$$f = \sin \pi x \sin \pi y,$$

and for SSW

$$f = (\sin \pi x - \tfrac{1}{6}\sin 2\pi x)(\sin \pi y - \tfrac{1}{6}\sin 2\pi y).$$

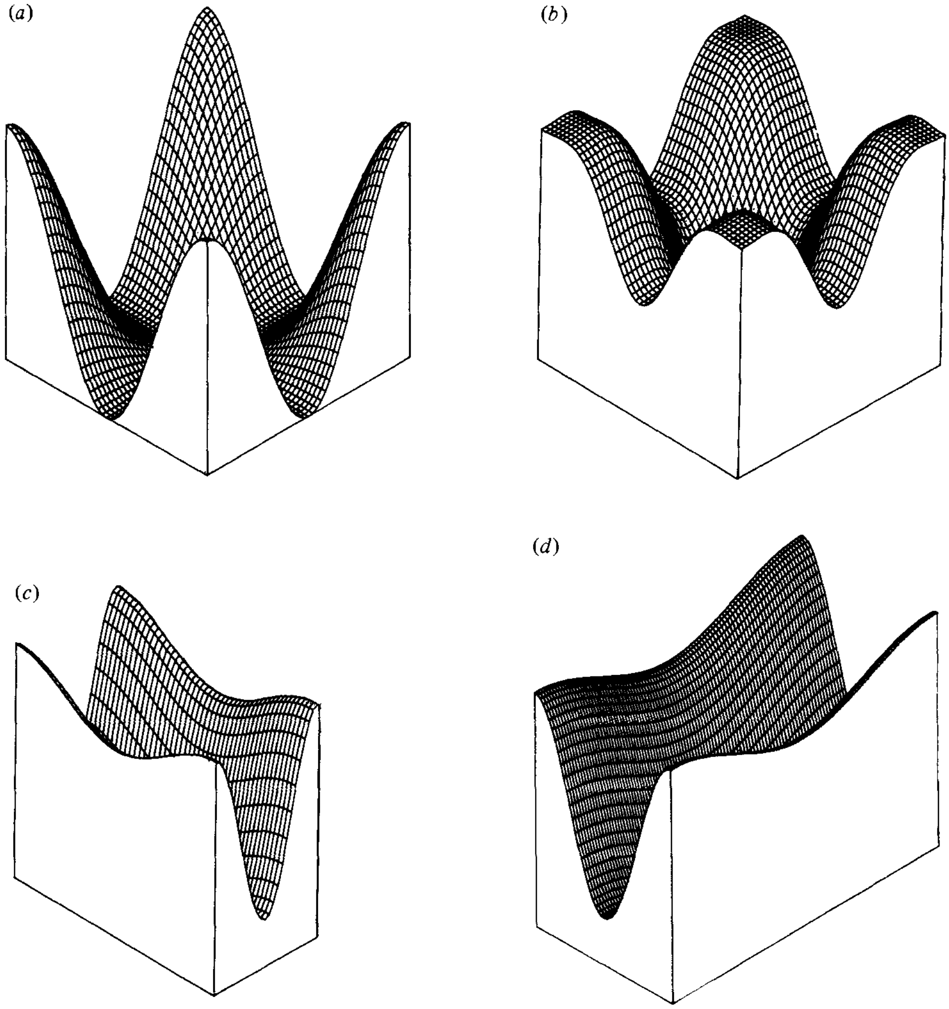

FIGURE 2. $u_z(x, y, \frac{1}{2})$ plotted as a surface of entire cell for velocity patterns (*a*) DY, (*b*) SSW, (*c*) $C_\parallel$ and (*d*) $C_\perp$. The left corner corresponds to the centre of the cell drawn in figure 1; the base plane is drawn at minimum u_z, i.e. not at $u_z = 0$.

Additionally we may seek surfaces $F(x,y) =$ constant. For DY, since $\partial h/\partial x$, $\partial h/\partial y$ are separable functions of x, y, elementary manipulation gives

$$F = \frac{\sin \pi x(1-\cos \pi x)\,(1+\cos \pi y)}{\sin \pi y(1-\cos \pi y)\,(1+\cos \pi x)} = \text{constant} \geqslant 0,$$

and there is a similar expression for SSW.

2.3. *Small-R_{m} theory*

Assuming $R_{\mathrm{m}} \ll 1$, the steady solution of (2.1) may be expressed as a power series in R_{m}, and the horizontally averaged magnetic field $\boldsymbol{B}_0 = B_0(z)\,\hat{\boldsymbol{x}}$ derived (appendix to DYM). First we deal with the irritating matter of how best to define R_{m}. We choose unit lengthscale and the maximum absolute value of dimensioned u_z to be the velocity scale. Thus here R_{m} is larger by the dimensionless peak value of u_z, $u_{z\mathrm{m}} = 3$, than in DYM, and a further factor π greater than Moffat's ϵ.

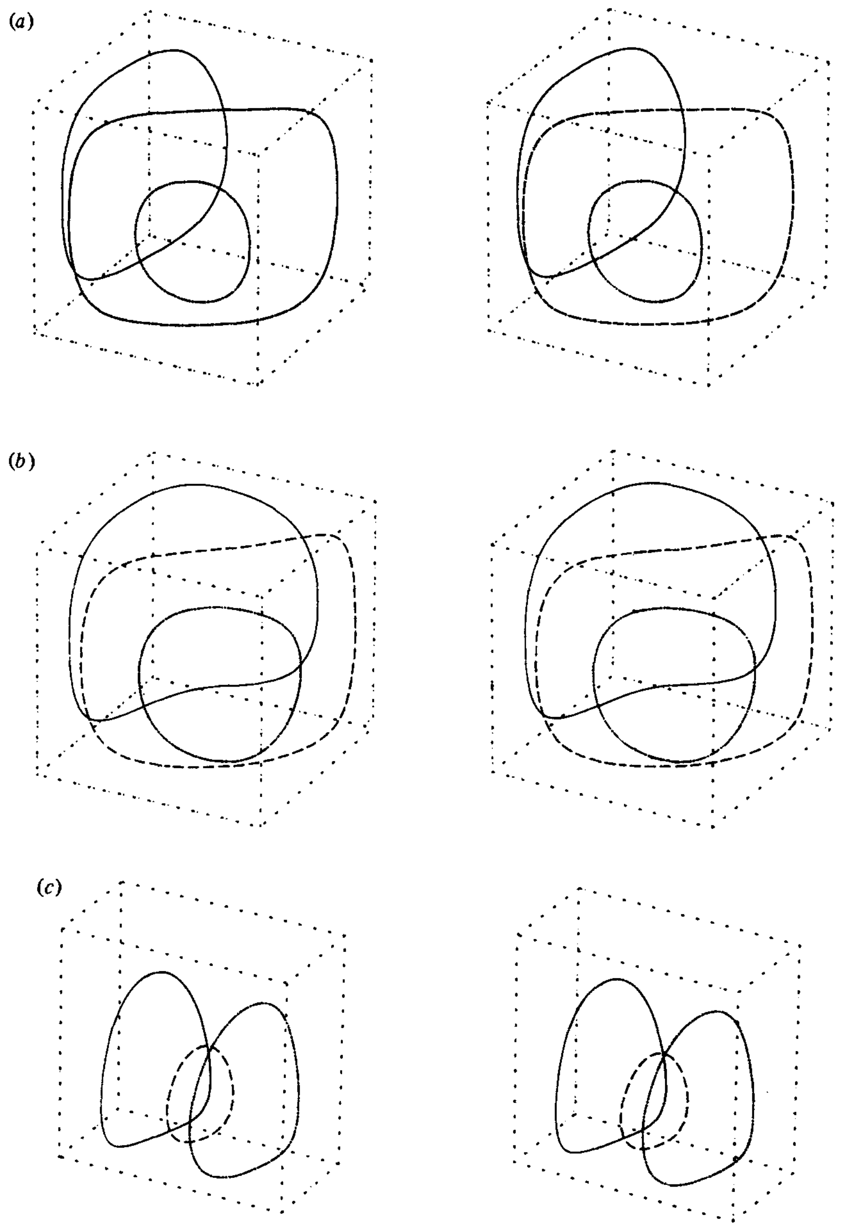

FIGURE 3. Stereo plot of quarter cell of symmetry (alignment illustrated in figure 1) showing streamlines of $\boldsymbol{u}$ for (*a*) DY, (*b*) SSW and (*c*) $C_{\parallel}$.

With this choice of R_{m} we have for DY

$$B_0(z) = 1+\frac{7}{432}\left(\frac{R_{\mathrm{m}}}{\pi}\right)^2 \cos 2\pi z+\frac{1}{6480}\left(\frac{R_{\mathrm{m}}}{\pi}\right)^3 (28\cos\pi z-3\cos 3\pi z)+O(R_{\mathrm{m}}^4), \qquad (2.2a)$$

and for SSW

$$B_0(z) = 1+\frac{423}{2880}\left(\frac{R_{\mathrm{m}}}{\pi}\right)^2 \cos 2\pi z-\frac{243}{102400}\left(\frac{R_{\mathrm{m}}}{\pi}\right)^3 (\cos\pi z-\cos 3\pi z)+O(R_{\mathrm{m}}^4). \qquad (2.2b)$$

The crucial result is the different sign of the coefficient of $R_{\mathrm{m}}^3 \cos \pi z$ in SSW, implying that flux rises rather than falls, although the whole term vanishes at $z = 0, 1$, unlike in DY. These transports represent the geometrical flux-pumping effect.

2.4. *Large-R_{m} theory*

This is more difficult, and no fully three-dimensional results have been derived (Childress 1979). We expect (Moffatt 1978) a flux tube of thickness $O(R_{\mathrm{m}}^{-\frac{1}{2}})$ to develop along the x-axis. Asymptotic theory shows that an initially $O(1)$ magnetic field is concentrated by a velocity field, (*a*) in two Cartesian space dimensions (x, z) into structures with form

$$B_z \sim R_{\mathrm{m}}^{\frac{1}{2}} \exp\left(-\frac{R_{\mathrm{m}} x^2}{L^2}\right), \tag{2.3}$$

and (*b*) with axisymmetry, coordinates (r, z), into

$$B_z \sim R_{\mathrm{m}} \exp\left(-\frac{R_{\mathrm{m}} r^2}{L^2}\right). \tag{2.4}$$

Writing the steady induction equation as $\boldsymbol{u} \wedge \boldsymbol{B} - R_{\mathrm{m}}^{-1} \operatorname{curl} \boldsymbol{B} = \operatorname{grad} \psi$, we see that when $\psi \equiv 0$ there is an approximate solution of the form

$$\boldsymbol{B} = \beta(R_{\mathrm{m}}^{p} \boldsymbol{x})\, \boldsymbol{u} - R_{\mathrm{m}}^{p-1}[\boldsymbol{\nabla}' \beta(R_{\mathrm{m}}^{p} \boldsymbol{x}) + \boldsymbol{b}(R_{\mathrm{m}}^{-1} \boldsymbol{x})] \tag{2.5}$$

for any p and function β, provided that $\boldsymbol{u} \wedge \boldsymbol{b} - \operatorname{curl}' \boldsymbol{b} = 0$. (A single prime denotes differentiation with respect to the function argument). By analogy with (2.3) and (2.4) we expect $p = \frac{1}{2}$, and for $p < 1$ the term in $\boldsymbol{u}$ dominates. Then $\operatorname{div} \boldsymbol{B} = 0$ and $\operatorname{div} \boldsymbol{u} = 0$ together imply $\boldsymbol{u} \cdot \operatorname{grad} \beta = 0$: not only is each fieldline identical with a flowline, but $|\boldsymbol{B}|/|\boldsymbol{u}|$ is constant along each line. Note that this last result necessarily fails for compressible flow.

Another useful result concerns $\Phi_1 = \Phi(x, \Lambda, z)$:

$$\frac{\partial \Phi_1}{\partial t} = -R_{\mathrm{m}}\left(\int_0^{\Lambda} [u_z B_x - u_x B_z]\, \mathrm{d}y\right) + \int_0^{\Lambda} j_y\, \mathrm{d}y, \tag{2.6}$$

where $\boldsymbol{j} = \operatorname{curl} \boldsymbol{B}$. In the large-$R_{\mathrm{m}}$ limit, provided that $\boldsymbol{B}$ does not vary too rapidly on the line of integration, the second term is negligible. Now, if $u_x = 0$ and u_z is everywhere negative on a surface (for DY, SSW this is the case for $x = \lambda$), steady-state B_x must change sign on lines $z = \text{constant}$, and indeed on every path outside boundary layers of $\boldsymbol{B}$ joining two opposite edges of a face. This point will be further discussed, but for the moment we remark that DYM do not consider the possibility that B_x may change sign.

2.5. *Compressible velocity fields*

We generalize the velocity fields of §2.2 by writing $v(z)$ for $\sin \pi z$. To satisfy $\operatorname{div} \boldsymbol{u} = cuz$, i.e. to give an anelastic velocity field in the density distribution $\rho(z) = \exp(-cz)$, we must add a term to $\boldsymbol{u}$ so that

$$\boldsymbol{u} = \operatorname{curl} \operatorname{curl}\, (g(x, y)\, v(z)\, \hat{\boldsymbol{z}}) + c \operatorname{grad}\, (g(x, y))\, v(z).$$

To within a positive normalization factor, the second-order term $B_0^2(z)$ in the expansion of $B_0(z)$ is found to satisfy

$$\frac{\mathrm{d}B_0^2}{\mathrm{d}z} = -\langle \nabla^2 g_{xx} \{v \Delta(g v') + v' \Delta(g v)\}\rangle + c \langle (g_{xx} v)\, \Delta(g_{xx} v) - (g_{yy} v)\, \Delta(g_{yy} v)\rangle, \tag{2.7}$$

where Δ denotes $-\nabla^{-2}$ and angle brackets horizontal averages.

The term in c (zero for incompressible flows) shows an asymmetry in the flux transport – velocity cells extended along the fieldlines will send flux in the opposite direction to those extended at right-angles to the field (the effect vanishes for cells of square planform). Setting $v(z) = \sin \pi z$ (a cubic sine could be used to make the velocity satisfy stress-free boundary conditions, but this should not be significant), $g(x, y) = \cos n\pi x + \cos m\pi y$, shows that field goes up in the first case. We denote the pattern with $n = 1, m = 2$ by $C_\parallel$, and that with $n = 1, m = \frac{1}{2}$ by $C_\perp$ ($C_\perp^*$: $n = 2, m = 1$ will also be discussed in §4.4). Flowlines of $C_\parallel$ are plotted in figure 3(c); $C_\perp$ is similar ($C_\perp^*$ identical) but oriented differently with respect to the initially imposed field. As in §2.2 the streamlines can be shown to be closed: they lie at the intersection of surfaces

$$\sin m\pi x \sin n\pi y \, v(z) \exp(cz) = \text{constant}$$

and

$$|\tan \tfrac{1}{2}m\pi y|^{n^2} \, |\tan \tfrac{1}{2}n\pi x|^{-m^2} = \text{constant} \geqslant 0.$$

3. Computational Techniques

3.1. *Numerical methods*

As in two dimensions, the induction equation may be solved numerically by using centred finite-difference schemes, with the DuFort–Frankel representation for diffusive terms (Roberts & Weiss 1966). The problem can then be naturally expressed in terms of a parallel numerical algorithm $O(N)$, where N is the number of mesh points used.

The ICL DAP (see e.g. Hockney & Jesshope 1981) provides a cost-effective means of handling such problems, and DAP-FORTRAN a natural means of coding them. If the degree of parallelism of the computer $P < \frac{1}{2}N$ (and for the DAP $P = 4096$), it is possible to exploit the symmetries of the difference scheme (S. F. Reddaway, private communication) so that use of a leapfrog method, where only alternate points are updated at each timestep, causes no loss of efficiency.

As a feasibility study, a straightforward code independently updating primitive variables B_x, B_y and B_z was written. This with y- and z-dependences separately suppressed was successfully checked for $R_\text{m} = 0.1, 1$ and 100 against a two-dimensional code run on a serial computer. A computation with x-dependence absent was by error started from a state with $\operatorname{div} \boldsymbol{B} \neq 0$, but (as must be the case when $\operatorname{div} \boldsymbol{u} = 0$) a uniform field was the outcome. Indeed for the fully three-dimensional runs, if $r = |\operatorname{divn} \boldsymbol{B}|_\text{max}/|\boldsymbol{B}|_\text{max}$, where divn is the second-order centred-difference form of the divergence, then using single-precision computer arithmetic $r \lesssim 10^{-5}$ was observed at all R_m for runs starting with $\operatorname{divn} \boldsymbol{B} = 0$. It becomes obvious with hindsight that divn $\boldsymbol{B}$ is subject purely to decay. Thus it is unnecessary to constrain it explicitly, and this code was used for all the runs described in §4. The mesh size was $24 \times 24 \times 24$ ($N = 13824$), representing one-quarter of a convective cell, except for $C_\perp$ and $C_\parallel$, where $24 \times 48 \times 24$ and $24 \times 12 \times 24$ meshes respectively were used. (A run was also made with a $16 \times 16 \times 16$ mesh as a check.) One timestep typically took 0.16 s and each run 1000–2000 timesteps. The DAP is being enhanced so that it will soon be possible to use a $60 \times 60 \times 60$ mesh.

3.2. *Presentation of results*

It is difficult to know how best to visualize fully three-dimensional vector fields. We can look at selected fieldlines in two-dimensional sections (Galloway & Proctor 1982, hereinafter referred to as GP), but there is no clear choice for such a plane here, apart from the boundaries, in terms of symmetries of $\boldsymbol{B}$. It is therefore necessary to project from three dimensions. Fortunately the GINO-F package (Computer Aided Design

Nominal	DY	SSW
3	3	2.7
5	6	5.3
10	12	10.7
25	24	21.3
50	48	42.7
100	96	85.3
150	144	128
200	192	170.7

TABLE 1. Exact values of R_m, defined in terms of peak velocity u_{zm}, used in the numerical calculations

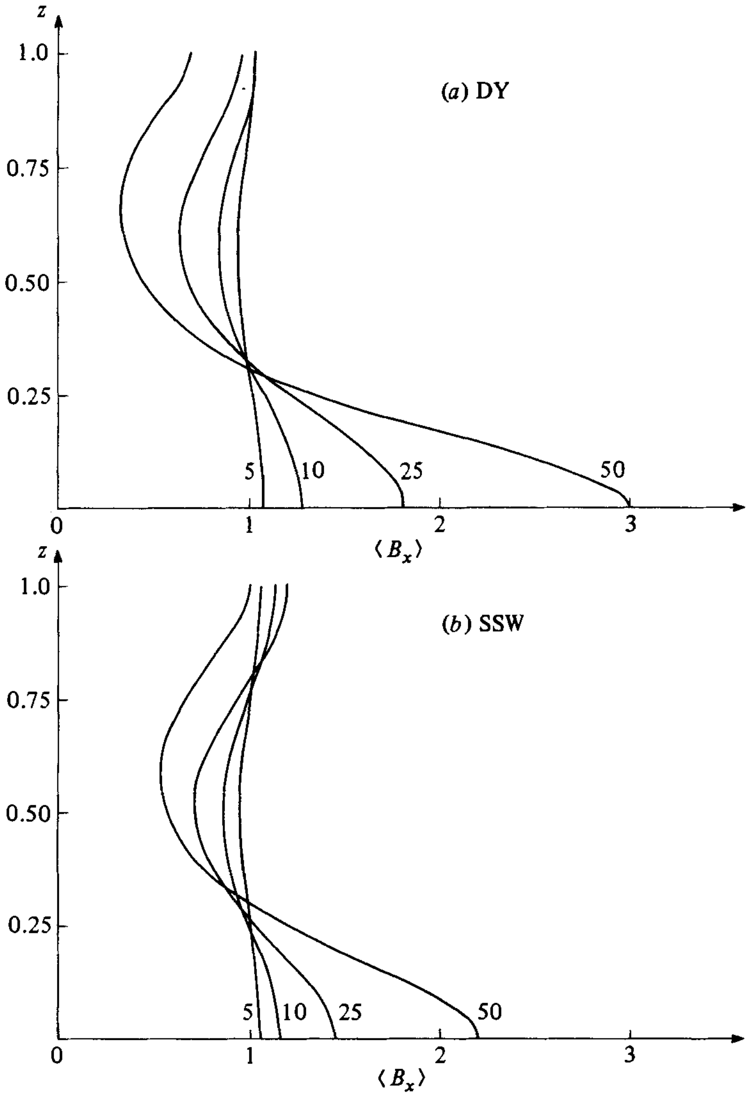

FIGURE 4. Plots of $B_0(z)$, horizontally averaged B_x, for velocity patterns (a) DY and (b) SSW with R_m up to 50. The values of R_m are marked on the curves.

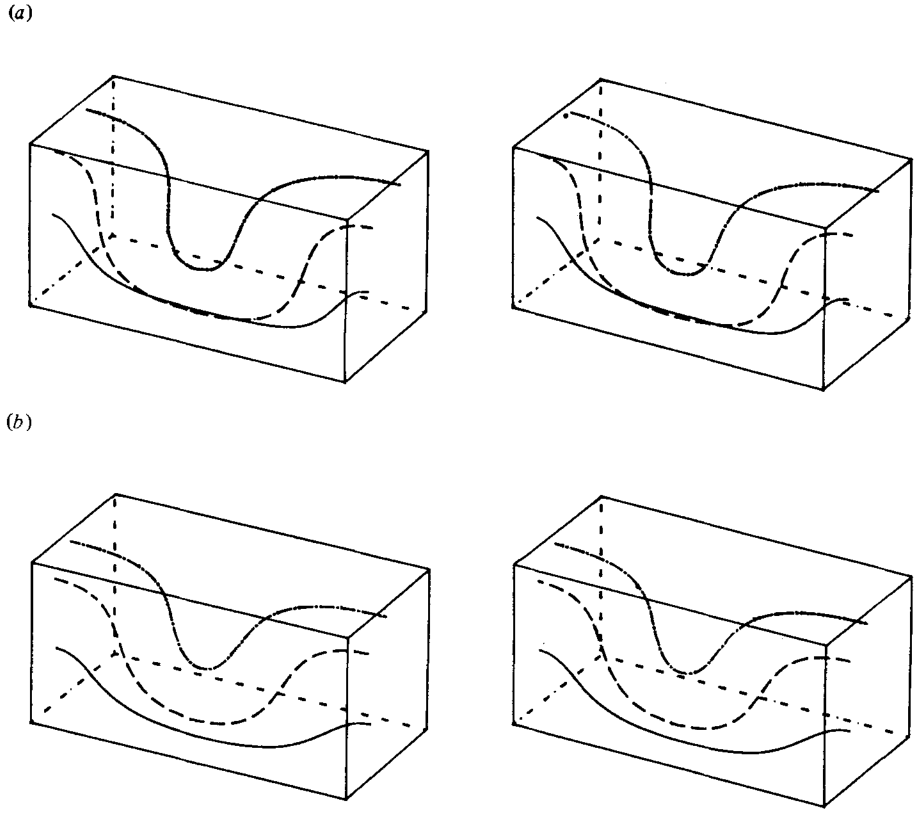

FIGURE 5. Stereo plot of the volume spanned by the base shown hatched in figure 1, showing lines of $\boldsymbol{B}$ for the steady-state $R_{\mathrm{m}} = 25$ in (*a*) velocity pattern DY, (*b*) velocity pattern SSW.

Centre, Cambridge) can handle the transformations involved, although it lacks facilities for hidden-line removal. Such a line-tracing code is then easily derived from GP's two-dimensional graphics, and stereo pairs may be produced.

Stereopsis is discussed in, for example, Gaunt & Gaunt (1978). Stereo viewers are helpful – a good deal of practice may otherwise be required to achieve the effect, and an unlucky ten percent of the population fails even with aids. The principle is to present two slightly different images of an object, corresponding to the views that would be seen by each eye independently if the object were, say, 25 cm away. Holding a stereo pair at about 15–30 cm distance, one half before each eye, stereopsis is achieved by relaxing the eyes so they focus on infinity. The observer in effect goes cross-eyed in such a way that two (of what would be four) images overlap. This (central) image, which may first appear out of focus, gives an accurate impression of depth.

Fieldlines can give a crude indication of field strength, but only when started from points equispaced throughout the cube volume. It proves useful to plot energy surfaces (again using GINO-F), which also facilitates comparison of output at different R_{m}. Attempts to simulate optical depth tracers, but using one primary colour for each of (three) intensity ranges, proved unsuccessful, partly owing to inadequate display hardware. The use of colour, to distinguish fieldlines and different energy levels viewed in projection, is extremely useful, but sadly too expensive to reproduce in this journal. The general graphical problem would repay further study.

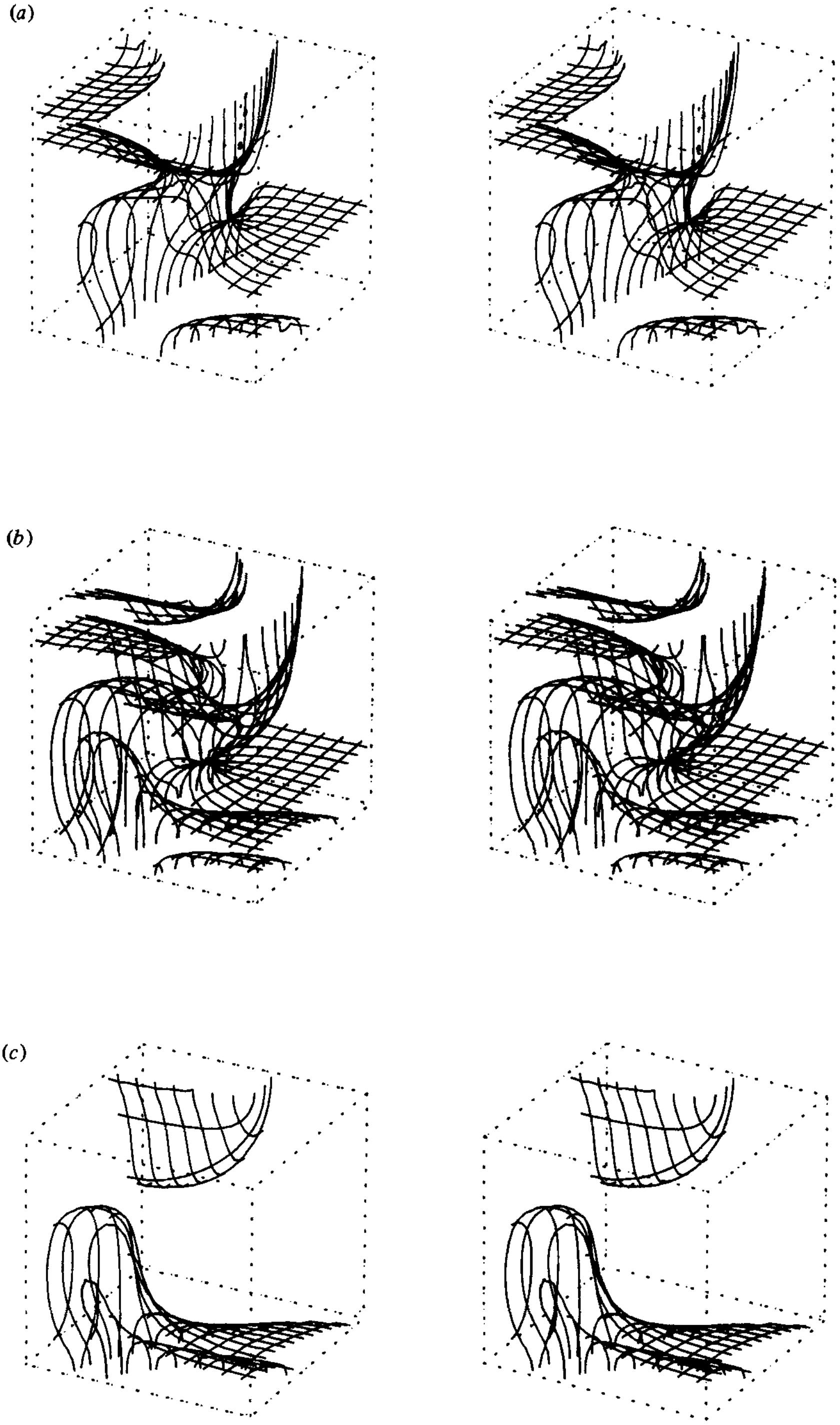

FIGURE 6(*a*–*c*). For caption see facing page.

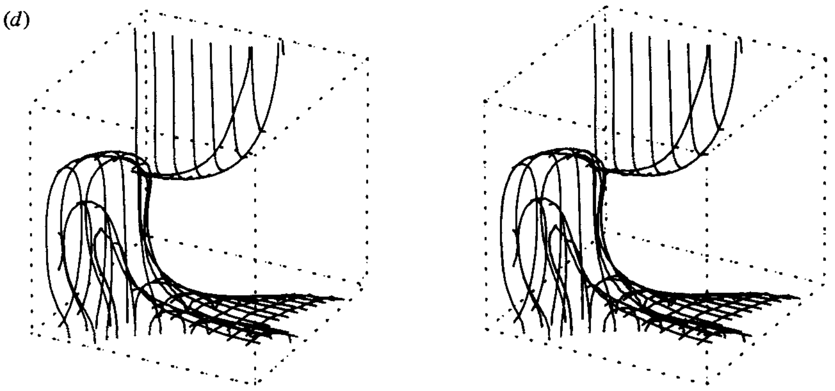

FIGURE 6. Stereo plot of the quarter-cell of symmetry, showing surfaces where energy $E(=B^2)$ = constant for $R_m = 100$ at intervals of time t_0, starting at time t_0. In, for example, (*a*), the higher energy surface $E = 5$ is disconnected: parts lie in the bottom near corner and the top left corner. The surface $E = 25$ appears in (*b*) in the near corner, and for the sake of clarity $E = 1$ is not shown in (*c*) and (*d*). The corresponding velocity pattern is DY.

4. Detailed numerical results

4.1. *Lower magnetic Reynolds number*

The computations presented in this subsection are for $R_m \leqslant 50$. Throughout it and §§4.2 and 4.3, nominal rounded values of R_m are given, to facilitate comparison between the different velocity patterns considered – the exact values used (definition in §2.3) are listed in table 1.

At these lower values of R_m, diffusion dominates and the equilibrium magnetic-field structure is little changed from its initial uniform state. This is also the range covered by DYM. For comparison, the steady values of $B_0(z)$ (the horizontally averaged x-component of the magnetic field) for the DY velocity pattern are plotted in figure 4(*a*), for R_m up to 50 – the equivalent of $R_m = 16$ in DYM. This reveals excellent agreement between solutions obtained using two quite different numerical schemes. In addition, note the development with increasing R_m of asymmetry about $z = \frac{1}{2}$ in $B_0(z)$.

In contrast, for SSW, $B_0(z)$ is approximately symmetric until $R_m = 50$, as shown in figure 5(*b*). The difference is expected by inference from the analytical results in §2.3. Figure 5 demonstrates that, before reconnection sets in, the broad, disjoint regions of rising flow in SSW are able to transport almost as much flux upwards as the narrower but linked regions of falling flow take down.

We conclude that topological effects are relatively unimportant at low R_m, and it is the detailed geometry of the flow which determines the $B_0(z)$ profile. This was suspected by Proctor (1975).

4.2. *Time-dependent behaviour*

Each computer run was started from a state with uniform horizontal magnetic field, and maximum values of B_x, B_y and B_z, plus the total magnetic energy E_{tot} were printed at each timestep. Almost without exception they increased monotonically toward the final steady state, and ultimately reached it exponentially on a diffusive timescale.

The runs with velocity patterns DY and SSW for $R_m = 100$ were studied in more

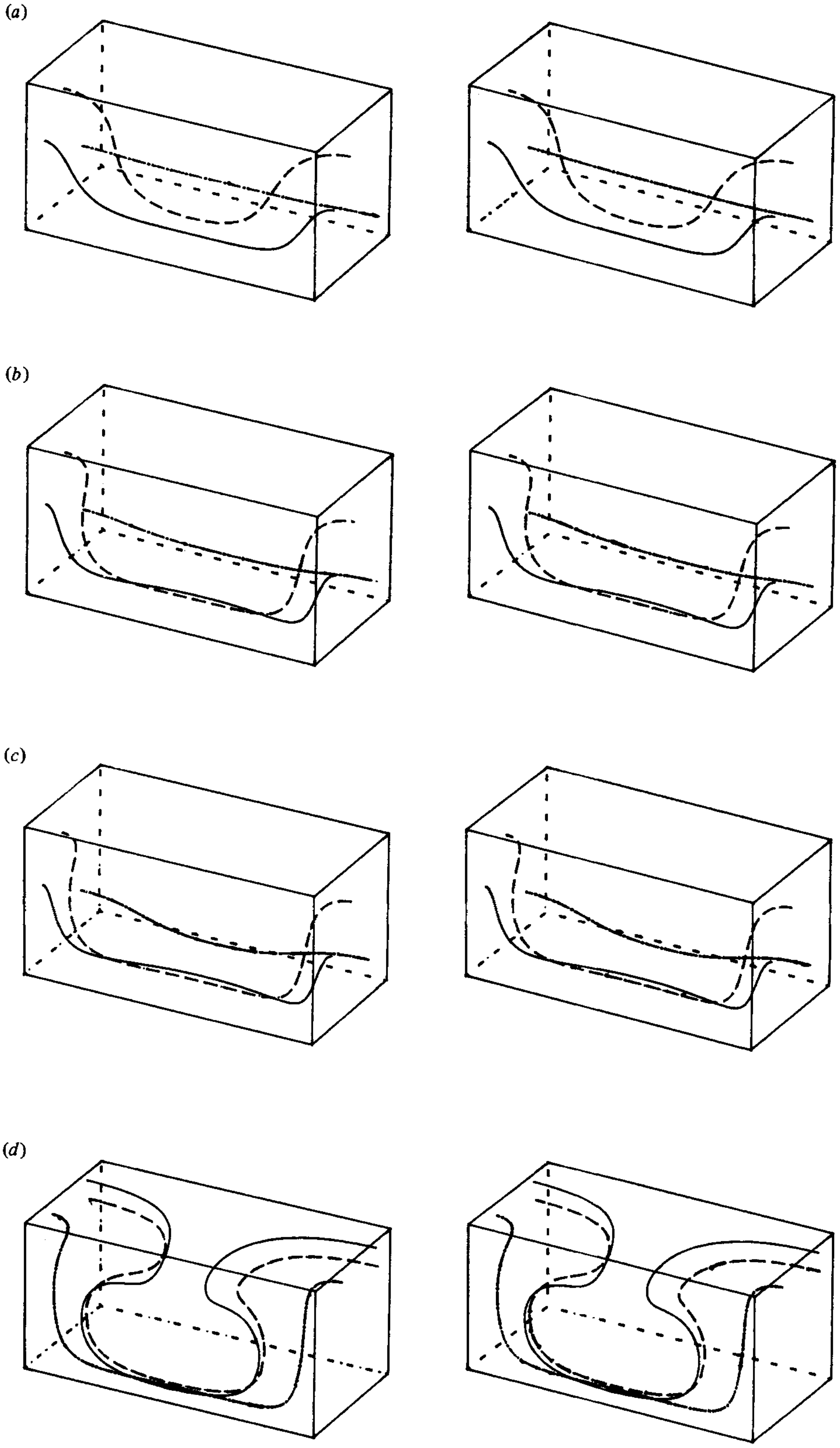

FIGURE 7(*a–d*). For caption see facing page.

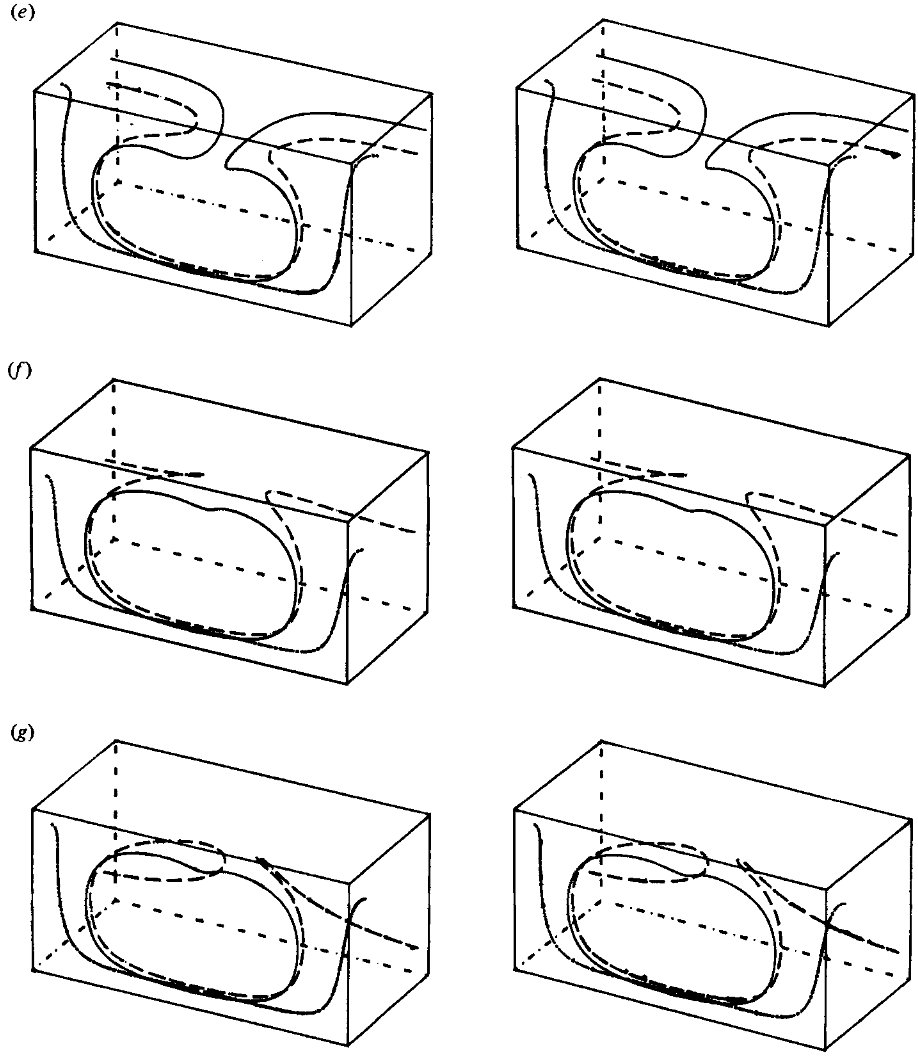

FIGURE 7. Stereo plot of fieldlines for $R_m = 100$, at intervals of time t_0. (*a*) is drawn at time t_0. (*a*)–(*c*) have fieldlines started at points on the face $x = 0$; (*d*)–(*g*) have lines started at points near the lower right-hand centre, inside the flux tube at $x = 1$; (*d*), like (*c*), is drawn at time $3t_0$. Corresponding velocity pattern is DY.

detail: the $\boldsymbol{B}$-field was saved at intervals of $t_0 = 1/u_{zm}$. (There is no unique definition of turnover time for the eddies – this is the smallest possible choice.) After time $2t_0$ the magnetic energy density E-contours already show greater concentration at the bottom of the cell (figure 6), and at time $3t_0$ the flux at the top is significantly reduced, having peaked at time $2t_0$, when the whole vertical distribution was nearly symmetric. By time $3t_0$ the field has bottlenecked in the volume where fluid rises – fieldlines have become so distorted there that rising field is reduced due to diffusive losses (see figures 7*a*–*c*). Other fieldlines may lie entirely in a region of falling fluid; less distortion accompanies their downward transport, which is thus more efficient, and flux builds up at the cell bottom. This corresponds, so far, to the description in DYM of 'topological pumping'. In this way, on a timescale of order of the turnover time, a bottom flux tube develops.

Reconnection however now begins, and not in the manner described in DYM. Instead of loops forming in the upper part of the cell by reconnection in or near the rising fluid, fieldlines merge in the falling fluid, leaving a nearly horizontal line plus a loop as much in the lower as in the upper part of the flow (figures 7*d*,*e*). Reconnection is largely finished by time $6t_0$ at $R_{\mathrm{m}} = 100$ (figures 7*f*,*g*). The field near the centre is reduced by being whirled away, by what locally amounts to a displacement.

Other lines are twisted into helices by the flow, in the same way that rotating a circular cylinder of variable radius, placed obliquely across a sticky string with free ends lying on a horizontal table, winds that string into helices (figure 7*f*,*g*). The velocity pattern may be conceived as the cylinder bent to form a toroid centred on the set of interior points where $\boldsymbol{u} = \mathbf{0}$, i.e. the cell axis.

The key feature is that motion is mainly oblique, but not perpendicular, to the imposed field: there is no analogue of the spirals in the two-dimensional problem (Weiss 1966), and the 3-dimensional vertical field problem (GP) shows little loop formation. A further distinction is that, for rolls, reconnection mainly occurs internally, not at the (cell) boundaries. Compare also the rotating-sphere problem (Parker 1966) in which the neutral points migrate inwards as the steady state is approached.

One last feature also noticed by Galloway & Proctor (1983) is that, as t is increased at constant R_{m}, $B_0(z)$ reproduces quite closely the steady-state profiles found at lower, but increasing, R_{m}: the low-t, high-R_{m} results are similar to the low-R_{m} results at large times. We may crudely demonstrate the equivalence using the approximation $|\delta \boldsymbol{B}| \ll 1$ (cf. the quasilinear approximation). We find for small t that B_0 varies as $\mathrm{e}^{R_{\mathrm{m}} t}$, but it remains somewhat mysterious that the equivalence apparently holds at larger times.

4.3. *Steady states at high R_{m}*

The steady field structures for DY and SSW are very similar at high R_{m}, as reflected by the $B_0(z)$ profiles in figure 8, indicating that geometrical effects are no longer important. The dominant feature of the results is a bottom flux tube running along the x-axis, parallel to the applied field and dividing the (entire) cell bottom into two (figure 9). Analysed in detail, it shows a Gaussian profile near $x = 1$, as would be expected from §2.4. However, DY is not locally axisymmetric, unlike SSW, so that the fall-off is more rapid in one normal direction than the other. In either flow, of course, as x decreases, the tube cross-section becomes more elongated in the vertical. The structure at $x = 1$, comparing $R_{\mathrm{m}} = 50$, 100, 150 and 200, asymptotes to

$$B_x \sim R_{\mathrm{m}}^{\frac{3}{2}} \exp\left[-R_{\mathrm{m}}\left(\frac{y^2}{L^2} + \frac{z^2}{M^2}\right)\right], \tag{4.1}$$

where for SSW $L \approx M \approx 1.7$, and for DY $L \approx 2.0$, $M \approx 1.4$.

The $\frac{3}{2}$ power-law dependence is surprising, particularly as this implies a positive flux along the tube $O(B_x R_{\mathrm{m}}^{-1}) \sim O(R_{\mathrm{m}}^{\frac{1}{2}})$. The net flux Φ_0 across any plane $x =$ constant is, though, constrained to be exactly unity, so there must be a negative flux $O(R_{\mathrm{m}}^{\frac{1}{2}})$ to compensate.

The energy contours in figure 9 show the development of a splayed feature at the top of the layer. We expect from (2.3) that as we follow fieldlines from the tube to this region and the field spreads out in the y-direction, its intensity will be reduced by $O(R_{\mathrm{m}}^{\frac{1}{2}})$ to $O(R_{\mathrm{m}})$. The field direction is reversed (figure 10), and, to make $\Phi_0 = 1$,

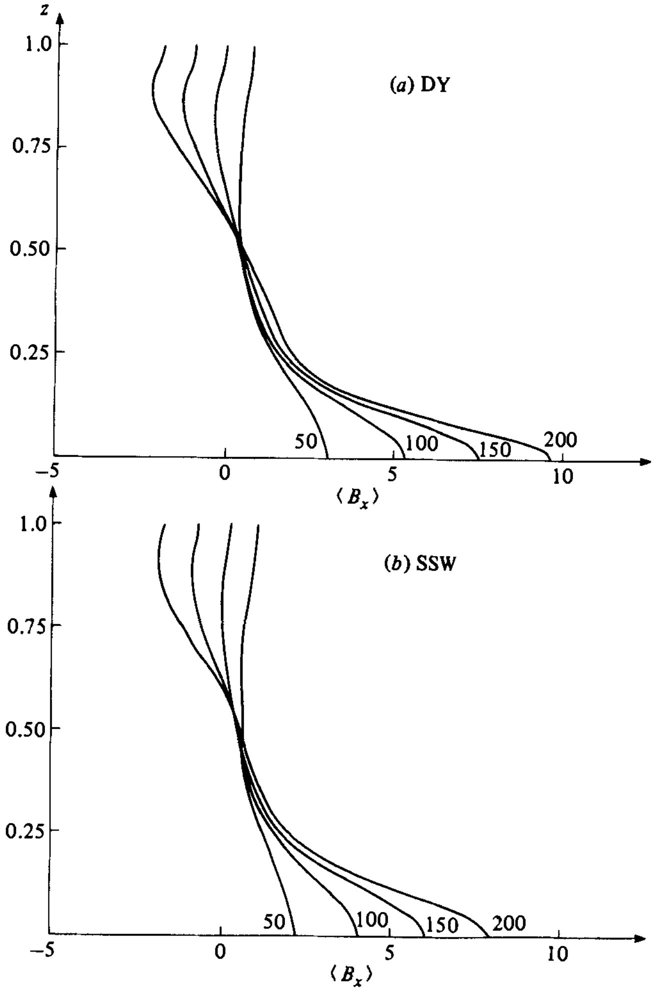

FIGURE 8. As figure 4, but for $R_m = 50$–200.

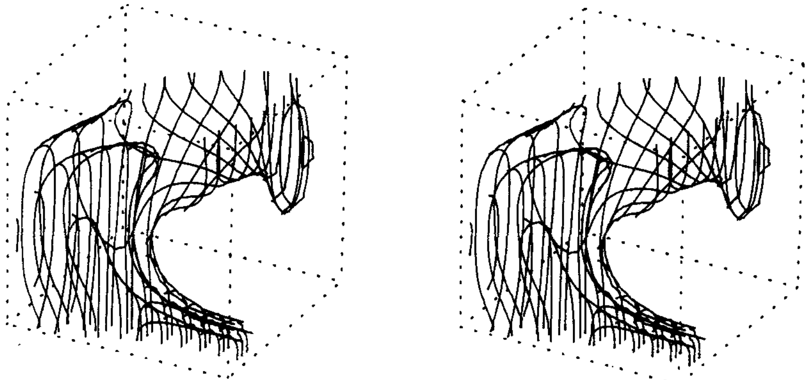

FIGURE 9. Stereo plot showing surfaces of constant energy $E = 25, 125, 625$ plotted for the steady-state field in the velocity pattern SSW with $R_m = 200$. The surface of highest E is innermost at the bottom near corner.

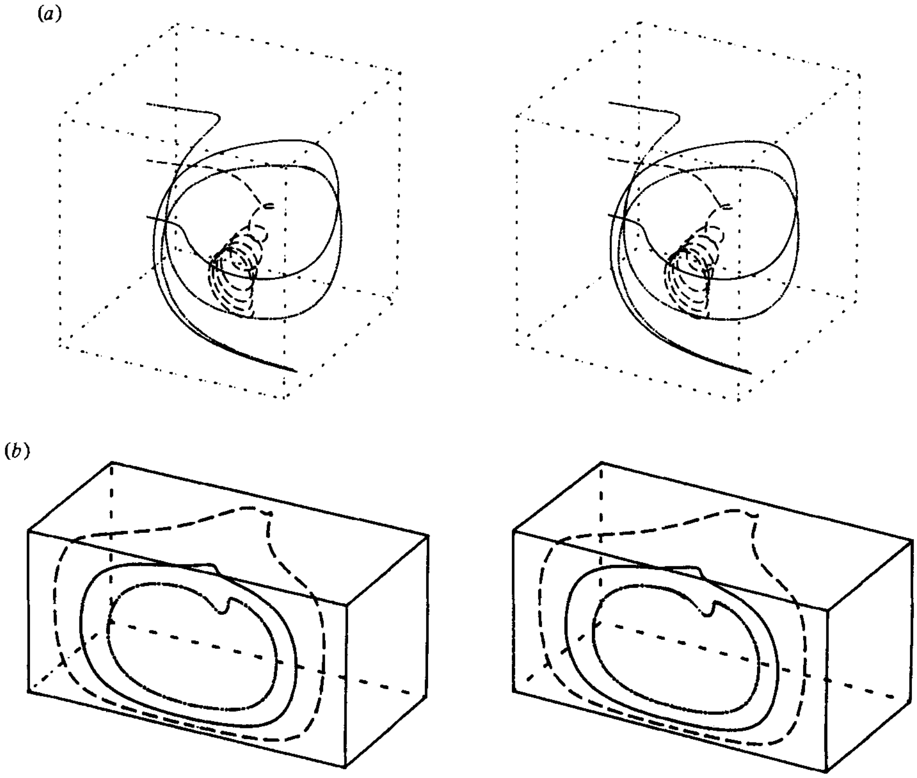

FIGURE 10. Stereo plot showing steady-state field in the velocity pattern SSW for $R_m = 200$ with (*a*) fieldlines started on the surface $x = 0$, and (*b*) started at points inside the flux-tube at $x = 1$.

must occupy an area $O(R_m^{-\frac{1}{2}})$. This is consistent with the numerical results, and indeed the flow near the top locally resembles that used in deriving (2.3) for the flux sheet.

It is necessary to sound a note of caution here: we may not be in the asymptotic regime as e.g. $E_{tot} = O(R_m^{2.3})$ rather than $O(R_m^2)$ as suggested by (4.1). Also, $R_m = 200$ may not be fully resolved by the $24 \times 24 \times 24$ mesh: the large size of B_x means, since $\operatorname{div} \boldsymbol{B} = 0$, steep gradients in B_y, B_z, and these components vary too rapidly in the tube. There may be more surprises in store at still higher R_m. However, Galloway & Proctor (1983) have performed similar computations for cells with hexagonal planform and found comparable behaviour for R_m up to 800.

The presence of closed loops of flux, at first sight rather mysterious, is a consequence of (2.6) and the imposed symmetry (§2.1). Without this symmetry there would be a component of $\boldsymbol{B}$ normal to the plane of the loops, which would turn them into helices.

Much of the fieldline structure can be explained by (2.5) and its consequences. On, say, $y = 0$, $|\boldsymbol{B}|$ mainly increases monotonically from its value at the cell axis, whereas $|\boldsymbol{u}|$ peaks at a distance, being zero on the axis by definition, and vanishing at the corners of the box. We see in figure 10 that the variation in helical radius as fieldlines are followed away from near $y = 0$ is consistent with conservation of $|\boldsymbol{B}|/|\boldsymbol{u}|$ along their length, as predicted by (2.5) at leading order. Encouraged by this agreement we remark that, if lines of $\boldsymbol{u}$ lie in a plane and are closed, (2.5) with $\boldsymbol{b} = \boldsymbol{0}$ is the equation of a helix with $O(R_m^p)$ turns per unit length, where it is likely that $p = \frac{1}{2}$ (§2.4). Thus the enhanced flux is a consequence of an originally straight fieldline contributing

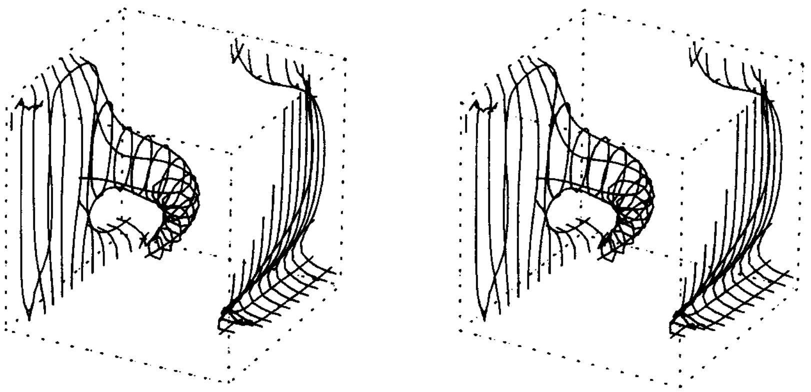

FIGURE 11. As figure 9, but the only energy surface plotted is $E = 1$, and the velocity pattern is DY, $R_m = 200$.

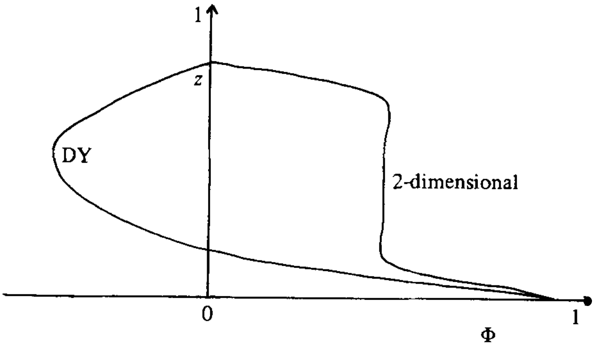

FIGURE 12. $\Phi_V = \int_V B_x \mathrm{d}V$, where V is the volume $z < \zeta < 1$, for typical 3- and 2-dimensional velocity patterns, $R_m = 150$.

$O(R_m^{\frac{1}{2}})$ times as it twists from $x = 0$ to $x = 1$, a point first realized intuitively by Proctor (private communication).

Finally, we ask to what extent is flux expelled from the flow? From figure 11 we see that the magnetic energy is low near the cell axis. This is merely a reflection of $|\boldsymbol{B}| \sim |\boldsymbol{u}|$, however, and there is a substantial amount of horizontal flux throughout the rest of the central part of the layer – indeed $|B_x| = O(1)$ close to the axis. The contrast with the flux distribution found for a velocity pattern consisting of two-dimensional rolls is very striking (figure 12). Of course the field outside the principal energy features is probably relatively as weak as in the two-dimensional calculations, but these results suggest that it does not vanish as $R_m \to \infty$.

4.4. *Steady states in compressible flows*

At high R_m the steady-state distributions of magnetic field in the velocity patterns $C_\perp$ and $C_\parallel$ differ markedly from each other, and from those discussed in §4.3. The essential features of all the steady states are, however, formed on a turnover timescale.

We see from figure 13 that in $C_\parallel$, where flow is predominantly around the direction of the imposed field (figure 2*c*), the lines of $\boldsymbol{B}$ are only slightly bent at $R_m = 100$, whereas in $C_\perp$ at the same R_m, their distortion is large and loops have formed,

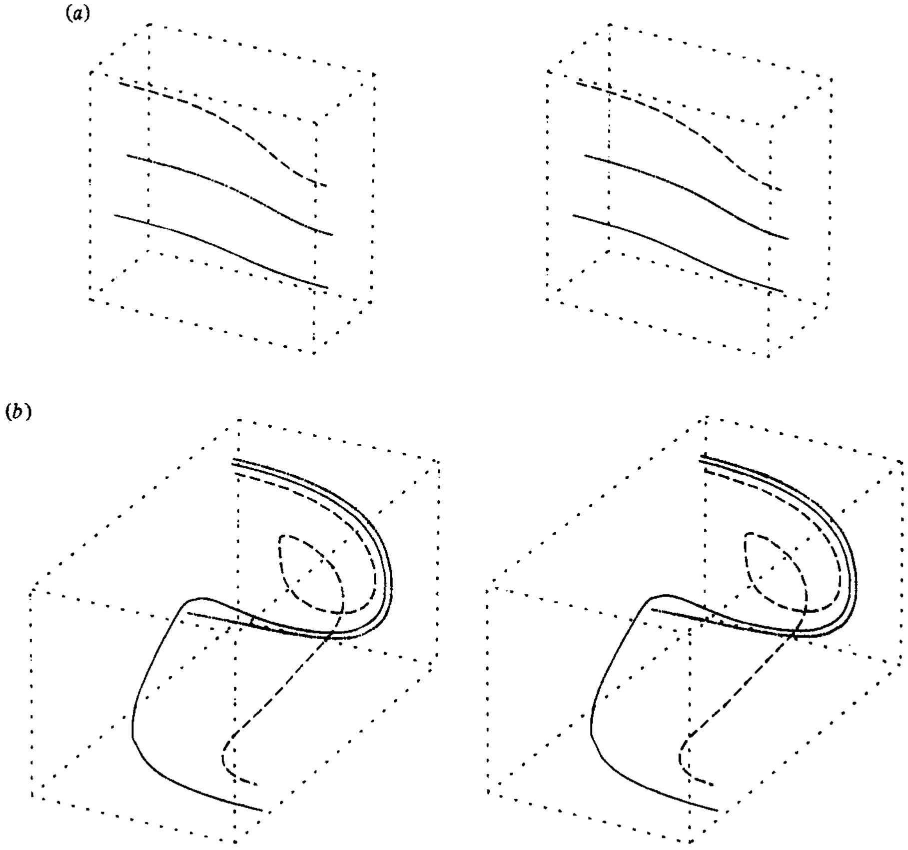

FIGURE 13. Stereo plot showing steady-state fieldlines at $R_m = 100$ for the velocity patterns (a) $C_\parallel$ and (b) $C_\perp$.

consistent with the analysis presented in §2.4. The energy contours in figure 14 suggest that flux has been transported upwards by $C_\perp$ and downwards by $C_\parallel$, as would be expected from (2.7). This is confirmed by the plots of $B_0(z)$ in figure 15.

It seems that, as in SSW and DY, there is enough motion oblique to the imposed field in $C_\perp$ (which, after all, is only elongated by a factor of two in planform) for flux enhancement to occur. Nevertheless, examination of the upper energy feature shows it to be tubelike, with a slow variation of $\exp(-x^2)$-form, and, as R_m increases,

$$B_x \sim R_m \exp\left[-R_m\left(\frac{y^2}{L^2}+\frac{z^2}{M^2}\right)\right]$$

for some L, M (cf. (2.3)). In addition, the total magnetic energy $E_{\text{tot}} = O(R_m)$; there is no evidence for an enhancement factor greater than $O(1)$. It may well be that $R_m \leqslant 100$ is not in the asymptotic regime.

The energy structure in $C_\parallel$ (figure 14b) is still more mysterious. Although at first sight it resembles a flux sheet, it does not have the $\exp(-z^2)$-type dependence. Indeed, the maximum value of energy is at $z = 0.25$ (on the left edge $x = 0$, $y = 1$), rather than on the bottom plane $z = 0$. Looking at the variation with R_m suggests that peak B_x,

$$B_{xm} = O(\ln R_m),$$

and

$$E_{\text{tot}} = 1.88 + O(R_m^{-1}).$$

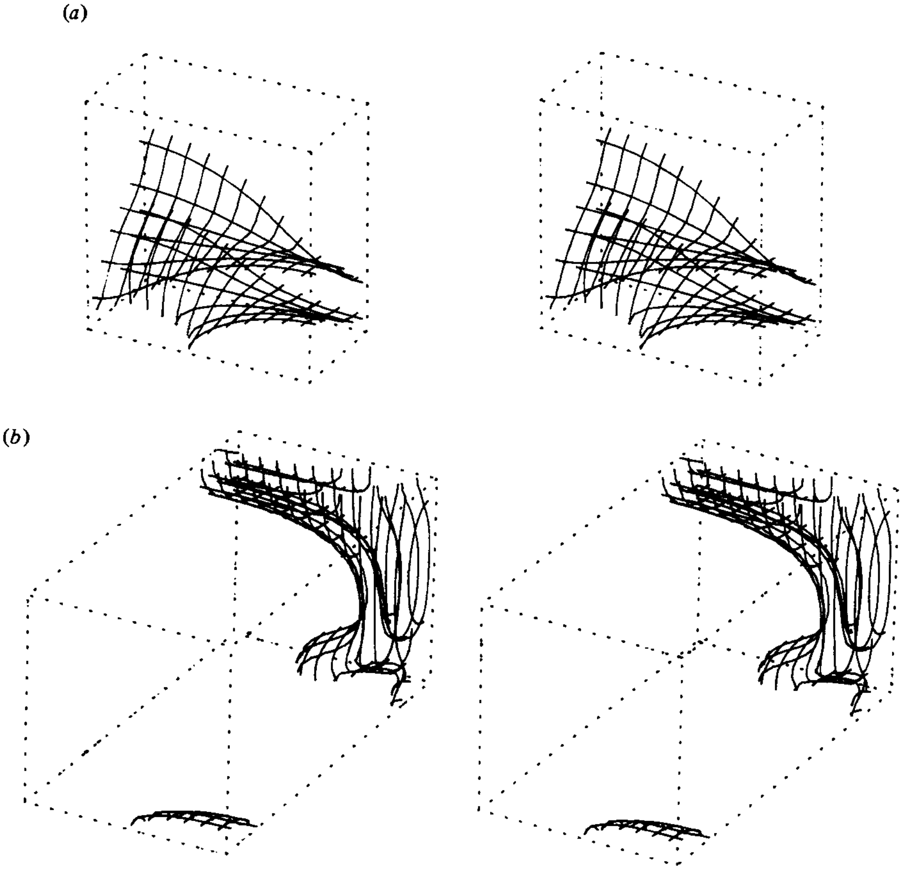

FIGURE 14. As figure 9, but for $R_m = 100$, and surfaces plotted are (*a*) $E = 1, 5$, velocity pattern $C_{\parallel}$; (*b*) $E = 10, 100, 1000$, velocity pattern $C_{\perp}$. In (*b*) the contour of highest energy is nearest the top far edge.

It must, however, be pointed out that asymptotic results for $C_{\parallel}$ are derived by considering only $R_m = 50, 100, 150$ and 200: other, more complex, R_m dependences are possible. Sadly, the mesh used, which has only 12 points in the y-direction, does not adequately represent $\boldsymbol{B}(\boldsymbol{x})$ when $R_m > 200$.

Hoping that calculations at higher R_m will confirm the above formulae, we also have for the minimum of $B_0(z)$

$$B_0(1) = 0.17 + O(R_m^{-1}).$$

This strongly suggests that the ratio of the flux in the lower half of the layer to that in the upper will, as R_m increases, stay near the value of 5:1 seen at $R_m = 200$. Decreasing c, equivalent to having more pressure scale heights across the layer, might lift this ratio further, but there is a competing geometrical effect, namely the 'roll' axis moves down to a height $z_a = -\pi^{-1}\tan^{-1}c^{-1}$. Incidentally, since $c = -1$ gives $z_a = \frac{1}{4}$, it is not too surprising that the flux is mostly found at the top in $C_{\perp}$. Presumably the bottom feature will mimic the top one as $R_m \rightarrow \infty$, although containing $O(1)$ less field.

What really needs explanation is the downward transport of flux by $C_{\parallel}$. Now when $c = 0$, $B_0(z)$ is symmetric with respect to $z = \frac{1}{2}$, so compressibility must be the key.

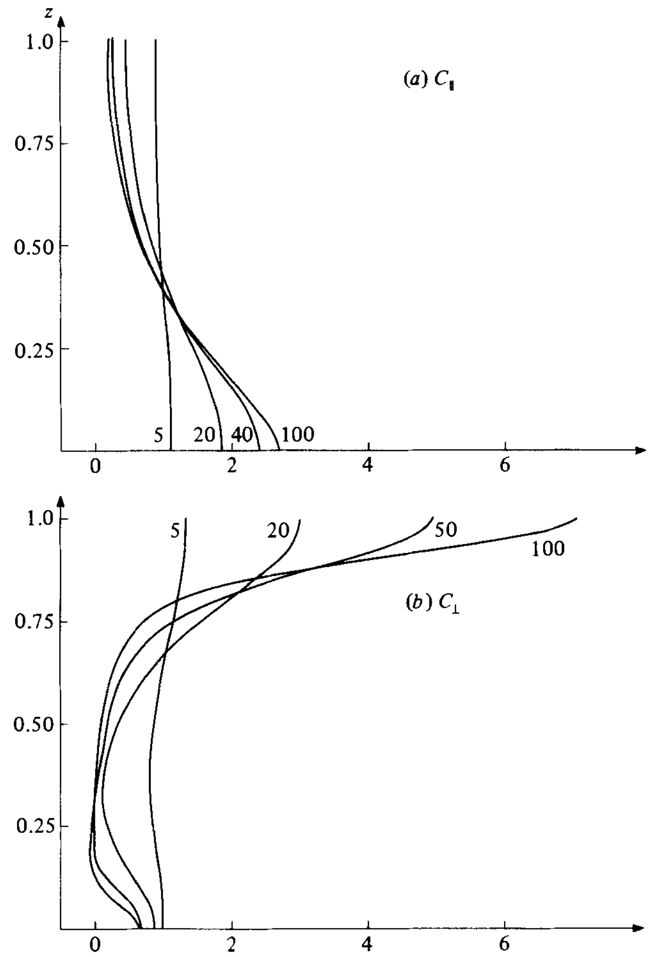

FIGURE 15. As figure 4, but drawn for velocity patterns (a) $C_\parallel$ and (b) $C_\perp$, for R_m up to 100.

If we expand the second term of the induction equation (2.1) we find

$$\operatorname{curl}(\boldsymbol{u} \wedge \boldsymbol{B}) = -(\boldsymbol{u} \cdot \operatorname{grad})\boldsymbol{B} + (\boldsymbol{B} \cdot \operatorname{grad})\boldsymbol{u} - \boldsymbol{B} \operatorname{div} \boldsymbol{u},$$

where by construction $\operatorname{div} \boldsymbol{u} = -cu_z$. Thus when $c < 0$ there is an additional term $\propto (-u_z)\boldsymbol{B}$, which implies field growth where $u_z < 0$, i.e. in descending flow. The increase in field strength is due to the concentration of the fluid with which the field is linked, or 'frozen to' in the limit $R_m \rightarrow \infty$ (Drobyshevski 1977; Moffatt 1978, chap. 3).

We should like to have shown that different directions of flux transport are produced simply by changing the alignment of the (compressible) convective pattern. The rotation of $C_\parallel$, $C_\perp^*$, was studied, but the mesh could not resolve field structure, which at $R_m = 100$ nevertheless resembled that of $C_\perp$ (which is not resolved for $R_m > 100$). The available evidence supports the conclusion that only a change in roll orientation is required to reverse the flux transport.

5. Relation to dynamo theory

The generation of net unsigned flux in §§4.2 and 4.3 leads us naturally to think of dynamo action, and particularly of the definition given by Hide (1979) in terms of $N(t) = \int_S |\boldsymbol{B}\cdot \mathrm{d}\boldsymbol{S}|$. The boundary conditions on $\boldsymbol{B}$ employed in this paper are however not such that we can safely call the DY velocity pattern a (semi)dynamo. Indeed, although Parker (1982) provides a simple model of a similar flux-generation process, for which he claims dynamo action, altering the boundary conditions to ones like those employed by dynamo theorists can drastically modify the behaviour of the system (Parker 1975; Arter, Galloway & Proctor 1982; Galloway & Proctor 1983).

We shall instead talk of flux enhancement, defined in the following way (after Hide 1979). Let S bound an entire convective cell (see figure 1). Then the fluid motions in the cell are said to enhance a flux of initially uniform field $N(0) = N_0$, if $N^* > 0$ and $N^*(t) \not\to 0$ as $t \to \infty$, where $N^* = N(t) - N_0$.

It is important that S be just that surface. Near $x = 0$, there is a layer where $B_x > 0$ for all y and z; thus there are always surfaces for which $N^* = 0$. Further, although in two dimensions N^* is non-zero away from cell boundaries (e.g. Weiss 1966) N remains $O(1)$, whereas here N increases to $O(R_\mathrm{m}^{\frac{1}{2}})$.

The small-R_m results (2.2) and (2.5) should also be looked at in the context of mean-field dynamo theory (Krause & Rädler 1980). The asymmetry in (2.2) corresponds to a third-order correlation (here meaning a non-zero horizontal average) in $\boldsymbol{u}$, the so-called γ-effect term, that of (2.6) to a second-order correlation described by Vainshstein (1978). Strictly speaking, Vainshstein uses the quasilinear approximation to derive high-R_m results, a procedure which is open to criticism (Parker 1979, chap. 17). The second-order α-effect term normally studied is zero, since by construction $\langle \boldsymbol{u}\cdot \operatorname{curl} \boldsymbol{u}\rangle = 0$; there is no net helicity after horizontally averaging, in any of the velocity patterns studied in this paper.

It is hard to relate the high-R_m results to the work of Krause & Rädler (1980), because the separation of scales required by mean-field electrodynamics does not exist in the vertical. If, following Drobyshevski, Kolesnikova & Yuferev (1980), we evaluate $\boldsymbol{E} = -\langle \boldsymbol{u} \wedge \boldsymbol{B}\rangle = (0, E_y(z), 0)$ we find that in the steady state $E_y = R_\mathrm{m}^{-1}\mathrm{d}B_0/\mathrm{d}z$ (except for regions near $z = 0, 1$ of thickness some negative power of R_m in DY, SSW), a result which might have been anticipated. Before the final state is reached, E_y and B_0 or its derivatives are not in simple proportion.

6. Conclusion

This study has shown that, for incompressible flows, topological effects dominate geometrical ones as R_m increases beyond about 50. It has provided more detailed discussion, with simple analytic explanations for the gross features, of results previously announced in abbreviated form by Arter (1982) and Arter *et al.* (1982). These are the generation of net unsigned flux in the form of loops and helices, and the consequent rebuttal of Drobyshevski & Yuferev's contention that all the flux is expelled from the top of a convecting layer. The proportion of field energy there does, however, become negligible as $R_\mathrm{m} \to \infty$, since it resides in a sheet, whereas there is a flux tube at the bottom.

The results for compressible flows are new. Roll-like motions with axis parallel to the imposed field can confine about 80% of the flux at their base: making the 'roll' axis normal to the field sends flux upwards. In the former situation the dominant mechanism appears to be field increase owing to the compression of the fluid that the fieldlines are 'frozen to'. In either case, it does not seem that flux can be wholly removed from half of a layer. Some of the field structures also remain enigmatic – it would be desirable to check the large-R_m behaviour by using larger grids when the computing power becomes available.

The implications of the incompressible results are not entirely clear. Assuming for the moment that we have here a good model of solar convection, which will be the more important for the global dynamo action, the flux or the energy in the magnetic field? Childress (1979) indicates that the α-effect due to flux sheets in a Cartesian geometry at high R_m is smaller than that due to flux tubes in an axisymmetric geometry; thus perhaps we should still expect the dynamo to be found at the base of the convection zone, as suggested by Galloway & Weiss (1981). (Although of course the velocity patterns discussed here have no net helicity, which, if included, could somewhat alter the picture.)

As for the validity of the model, the top boundary condition which does not allow field to escape was criticized by Parker (1975), and dropped for the reply (for R_m up to 50) produced by Drobyshevski *et al.* (1980). Unfortunately the method used here is not easily modified to repeat these latter calculations. Indeed, changing the boundary conditions can greatly affect the results. Galloway & Proctor (1983) impose a current-free atmosphere above the layer, and find that the magnetic flux decays, although on a long timescale $O(R_m^{\frac{1}{2}})$. Drobyshevski *et al.* (1980) additionally use the current-free condition underneath, to discover that flux is more completely expelled from the upper part of the layer than in DYM. This should be further studied.

The compressible results have shown up a process which could act rather imperfectly like flux pumping as originally envisaged by DYM. There are two likely alignments for a roll axis in the solar convection zone – parallel to the rotation axis and parallel to the predominantly toroidal field. The first will be preferred where the field is relatively weak and (cf. $C_\perp$) send flux upwards, the second only where the field is strong and (cf. $C_\parallel$) the motion will confine it, in agreement with Vainshstein (1978). However, for the latter to happen in the Sun the field would be so large that magnetic buoyancy would also be important (Parker 1979). Its effect should therefore be included in any realistic calculation.

The same remark applies to sunspot penumbrae, where convection takes place in a mainly horizontal field (Danielson 1961; McIntosh 1981). If the compression mechanism is dominant, we would expect to see magnetic field in regions of falling fluid. This process would then also reduce upward field loss from the penumbrae. We are on safer ground when we take DY, SSW or $C_\perp$ as model for the giant-cell solar convection – the implication is that flux enhancement may help to explain the persistence of the large-scale magnetic features (see McIntosh 1981); cf. also Parker (1982).

Finally, we remark upon the variety of behaviour possible in just four simple velocity fields. Since solar observations do not greatly constrain the choice of flow pattern, study of the fluid-dynamical problem, including a Lorentz-force term, might be a faster road to an understanding of the physics of solar convection. Work on such a problem, although neglecting magnetic-flux buoyancy, is currently in progress.

Thanks are due to Drs M. R. E. Proctor, N. O. Weiss and D. J. Galloway for useful and enlightening conversations. I wish also to thank the staff in general, and Dr G. S. J. Bowgen in particular, at DAPSU, Queen Mary College, London, for advice and assistance, and the SERC for both a studentship and time on the DAP. The

output of the DAP runs was analysed on the IBM 370/165 and IBM 3081 of the Cambridge University Computing Service.

REFERENCES

Arter, W. 1982 Topological magnetic flux pumping revisited. In *Proc. IAU Symp.* no. 102 (ed. J. O. Stenflo). To appear.

Arter, W., Galloway, D. J. & Proctor, M. R. E. 1982 New results on the mechanism of magnetic flux pumping by three-dimensional convection. *Mon. Not. R. Astron. Soc.* **201**, 57*P*–61*P*.

Arter, W. 1983 Non-linear convection in an imposed horizontal magnetic field. *Geophys. Astrophys. Fluid Dyn.* (in press).

Busse, F. H. 1977 Convection in rotating stars. In *Problems of Stellar Convection* (ed. E. A. Spiegel & J.-P. Zahn), Lecture notes in Physics, vol. 71, p. 157–175. Springer.

Busse, F. H. 1978 Non-linear properties of thermal convection. *Rep. Prog. Phys.* **41**, 1929–1967.

Childress, S. 1979 Alpha-effect in flux ropes and sheets. *Phys. Earth Planet. Int.* **20**, 172–180.

Cowling, T. G. 1982 The present status of dynamo theory. *Ann. Rev. Astron. Astrophys.* **19**, 115–135.

Danielson, R. E. 1961 The structure of sunspot penumbras II. Theoretical. *Astrophys. J.* **134**, 289–311.

Drobyshevski, E. M. 1977 Magnetic field transfer by two-dimensional convection and solar 'semi-dynamo'. *Astrophys. Space Sci.* **46**, 41–49.

Drobyshevski, E. M., Kolesnikova, E. N. & Yuferev, V. S. 1980 The rate of magnetic field penetration through a Bénard convection layer. *J. Fluid Mech.* **101**, 65–78.

Drobyshevski, E. M. & Yuferev, V. S. 1974 Topological pumping of magnetic flux by three-dimensional convection. *J. Fluid Mech.* **65**, 33–44.

Galloway, D. J. & Proctor, M. R. E. 1982 Flux expulsion in hexagons. In *Planetary and Stellar Magnetism* (ed. A. M. Soward). Gordon & Breach.

Galloway, D. J. & Proctor, M. R. E. 1983 The kinematics of hexagonal magneto convection. *Geophys. Astrophys. Fluid Dyn.* (in press).

Galloway, D. J. & Weiss, N. O. 1981 Convection and magnetic fields in stars. *Astrophys. J.* **243**, 945–953.

Gaunt, W. A. & Gaunt, P. N. 1978 *Three-dimensional Reconstruction in Biology.* Pitman.

Gilman, P. A. 1978 Linear simulations of Bossinesq convection in a deep rotating spherical shell. *J. Atmos. Sci.* **32**, 1331–1352.

Gilman, P. A. 1980 Global circulation of the sun: where are we and where are we going? In *Highlights of Astronomy*, vol. 5 (ed. P. A. Wayman), pp. 19–37. Reidel.

Gilman, P. A. 1982 Convective dynamos for rotating stars. Unpublished manuscript.

Gilman, P. A. & Miller, J. 1981 Dynamically consistent non-linear dynamos driven by convection in a spherical rotating shell. *Astrophys. J. Suppl.* **46**, 211–238.

Hide, R. 1979 On the magnetic flux linkage of an electrically conducting fluid. *Geophys. Astrophys. Fluid Dyn.* **12**, 171–176.

Hockney, R. W. & Jesshope, C. R. 1981 *Parallel Computers.* Adam Hilger.

Krause, F. & Rädler, K.-H. 1980 *Mean-field Magnetohydrodynamics and Dynamo Theory.* Pergamon.

McIntosh, P. S. 1981 The birth and evolution of sunspots: observations. In *The Physics of Sunspots* (ed. L. E. Cram & J. H. Thomas), pp. 7–54. Sacramento Peak Observatory.

Moffatt, H. K. 1978 *Magnetic Field Generation in Electrically Conducting Fluids.* Cambridge University Press.

Parker, E. N. 1975 The escape of magnetic flux from a turbulent body of gas. *Astrophys. J.* **202**, 523–527.

Parker, E. N. 1979 *Cosmical Magnetic Fields.* Clarendon.

Parker, E. N. 1982 The flux ejection dynamo effect. *Geophys. Astrophys. Fluid Dyn.* **20**, 165–189.

PARKER, R. L. 1966 Reconnection of lines of force in rotating spheres and cylinders. *Proc. R. Soc. Lond.* A **291**, 60–72.

PROCTOR, M. R. E. 1975 Non-linear mean field dynamo models and related topics. Ph.D. thesis, University of Cambridge.

PROCTOR, M. R. E. & WEISS, N. O. 1982 Magnetoconvection. *Rep. Prog. Phys.* **45**, 1317–1379.

ROBERTS, K. V. & WEISS, N. O. 1966 Convective difference schemes. *Math. Comp.* **20**, 272–299.

VAINSHSTEIN, S. I. 1978 Magnetohydrodynamic effects in a turbulent medium having nonuniform density. *Mag. Gidrodin.* **1**, 45–50 [English transl. *Magnetohydrodyn.* **1**, 36–41].

WEISS, N. O. 1966 The expulsion of magnetic flux by eddies. *Proc. R. Soc. Lond.* A **293**, 310–328.

WEISS, N. O. 1981 Convection in an imposed magnetic field. Part 1. The development of non-linear convection. *J. Fluid Mech.* **108**, 247–272.